



# Radio Follow-up on All Unassociated Gamma-Ray Sources from the Third *Fermi* Large Area Telescope Source Catalog

Frank K. Schinzel<sup>1,5</sup>, Leonid Petrov<sup>2</sup>, Gregory B. Taylor<sup>3,6</sup>, and Philip G. Edwards<sup>4</sup>

<sup>1</sup>National Radio Astronomy Observatory, P.O. Box O, Socorro, NM 87801, USA; [fschinze@nrao.edu](mailto:fschinze@nrao.edu)

<sup>2</sup>Astrogeo Center, Falls Church, VA 22043, USA

<sup>3</sup>Department of Physics and Astronomy, University of New Mexico, Albuquerque, NM 87131, USA

<sup>4</sup>CSIRO Astronomy & Space Science, P.O. Box 76, Epping, 1710 NSW, Australia

Received 2016 June 30; revised 2017 February 6; accepted 2017 February 20; published 2017 April 3

## Abstract

The third *Fermi* Large Area Telescope  $\gamma$ -ray source catalog (3FGL) contains over 1000 objects for which there is no known counterpart at other wavelengths. The physical origin of the  $\gamma$ -ray emission from those objects is unknown. Such objects are commonly referred to as unassociated and mostly do not exhibit significant  $\gamma$ -ray flux variability. We performed a survey of all unassociated  $\gamma$ -ray sources found in 3FGL using the Australia Telescope Compact Array and Very Large Array in the range 4.0–10.0 GHz. We found 2097 radio candidates for association with  $\gamma$ -ray sources. The follow-up with very long baseline interferometry for a subset of those candidates yielded 142 new associations with active galactic nuclei that are  $\gamma$ -ray sources, provided alternative associations for seven objects, and improved positions for another 144 known associations to the milliarcsecond level of accuracy. In addition, for 245 unassociated  $\gamma$ -ray sources we did not find a single compact radio source above 2 mJy within  $3\sigma$  of their  $\gamma$ -ray localization. A significant fraction of these empty fields, 39%, are located away from the Galactic plane. We also found 36 extended radio sources that are candidates for association with a corresponding  $\gamma$ -ray object, 19 of which are most likely supernova remnants or H II regions, whereas 17 could be radio galaxies.

*Key words:* catalogs – galaxies: active – gamma rays: general – radio continuum: general – surveys

*Supporting material:* machine-readable tables, tar.gz file

## 1. Introduction

The latest generation of  $\gamma$ -ray observatories, in particular the Large Area Telescope (LAT) aboard the *Fermi* satellite, have revolutionized the field of  $\gamma$ -ray astronomy. The previous major satellite mission, the Energetic Gamma-Ray Experiment Telescope on board the *Compton Gamma Ray Observatory*, detected only a couple of hundred point sources (Hartman et al. 1999; Casandjian & Grenier 2008). Since its launch in 2008 August, *Fermi*/LAT has detected thousands of distinct  $\gamma$ -ray-emitting objects, which have been reported in multiple catalogs. For all of these catalogs a significant fraction, typically  $>30\%$ , of the detected point sources have no known counterpart at any other wavelength and their nature is unknown. This makes the  $\gamma$ -ray sky the least understood in all of observational astronomy.

There are two ways to associate objects from different catalogs: (1) to match light curves if a source manifests variability; (2) to associate by proximity. Due to errors in the measurement of flux or localization, both methods are statistical. Association by proximity is based on two probabilities: the probability that entries in two catalogs are related to the same object with the difference in position being due to uncertainties in localization, and the probability that the second catalog contains a coincident background object, unrelated to the object in the first catalog. The second probability is crucial for effective association. If the catalog selected for association contains too many objects such that the probability of finding a background object within the localization error ellipse is not

small, then the effectiveness of association with such a catalog will be too low to be practical.

The method for source associations used in the 3FGL is addressed in Section 5 of Acero et al. (2015). A detailed description of the method can be found in Ackermann et al. (2012). We found in our previous work (Petrov et al. 2013; Schinzel et al. 2015) that association based on proximity of *Fermi* sources to radio sources with emission at 8 GHz at parsec scales is very effective. In this paper we will present the results from our method, which is complementary to the approach taken by the *Fermi* science team. Following the statistical criteria described in Petrov et al. (2013), the detection of a compact radio source brighter than 12 mJy at 8 GHz found within the  $2\sigma$  *Fermi* localization error ellipse establishes an association. More than 50% of all *Fermi* associations are made on the basis of this approach. There are two reasons why this method of association based on detection by very long baseline interferometry (VLBI) is so powerful. First, the number of compact radio sources is rather limited: according to the  $\log N$ – $\log S$  distribution, there are only 100,000 sources brighter than 10 mJy at parsec scales at 8 GHz (Petrov et al. 2013). Second, variability of both *Fermi*  $\gamma$ -ray sources and compact radio sources suggests that emission is contemporaneous and comes from regions on parsec scales. In contrast, catalogs from connected interferometers, such as NVSS (Condon et al. 1998) and SUMSS (Bock et al. 1999; Mauch et al. 2003), typically probe emission at kiloparsec scales that is related to the interaction of particles in the jet with surrounding media thousands of years ago.

Our approach is first to observe with connected interferometers fields within the *Fermi* localization error ellipse at 5–9 GHz and then follow up detected sources with VLBI. Emission from a compact core usually dominates at these frequencies, in contrast to frequencies below 2 GHz where emission from extended jets

<sup>5</sup> An Adjunct Professor at the University of New Mexico.

<sup>6</sup> An Adjunct Astronomer at the National Radio Astronomy Observatory.

or radio lobes generally dominates. Therefore detection of a source at arcsecond scales at 5–9 GHz increases the probability of finding detectable emission at milliarcsecond scales at 8 GHz. This contrasts to the case when only emission at 0.8–1.4 GHz at the arcsecond scale is known, which generally does not result in detection of compact emission. Observations with connected interferometers at 5–9 GHz serve as a screening tool for potential targets for follow-up VLBI observations to find new associations.

In 2012, we started a campaign to image *all* regions covered by the *Fermi* localization error ellipse that contain unassociated *Fermi* sources, first with connected interferometers at 4–10 GHz, then with VLBI. The results covering the second *Fermi* point source catalog (2FGL; Abdo et al. 2013) were reported in Petrov et al. (2013) and Schinzel et al. (2015). The 2FGL presented 1873 sources of which 575 were considered unassociated. Follow-up on those unassociated sources revealed 865 radio sources at arcsecond scales as candidates for association. We then obtained new associations using VLBI for 76 of the unassociated  $\gamma$ -ray sources with radio-loud active galactic nuclei (AGNs). We found that 129 out of 588 observed  $\gamma$ -ray sources at arcminute scales did not have a single radio continuum source detected above our sensitivity limit within the  $3\sigma$   $\gamma$ -ray localization. These “empty” fields were found to be particularly concentrated at low Galactic latitudes.

Since then, a third source catalog has been released by the *Fermi*/LAT collaboration (3FGL; Acero et al. 2015), covering the first four years of operations and listing 3033 sources, among which 1010 were reported to have no plausible counterpart at other wavelengths. Most of the identified or associated  $\gamma$ -ray sources are active galaxies. Here we present an update of our work that includes radio observations for new 3FGL unassociated sources and presents them in the context of our previous work.

The 2FGL catalog covers the first two years of the *Fermi*/LAT mission and lists all point sources found over that time period with about  $5\sigma$  sensitivity. At the time of publication it listed 575 unassociated point sources. However, since its release the catalog has been modified and the version released on 2015 May 18 contains 651 unassociated  $\gamma$ -ray sources with a median  $\gamma$ -ray flux density of  $1.21 \times 10^{-12}$  photons  $\text{cm}^{-2} \text{MeV}^{-1} \text{s}^{-1}$  and  $\gamma$ -ray spectral index of 2.31. In 3FGL, covering the first four years of the *Fermi*/LAT mission, the number of unassociated sources listed as of 2015 May 18 had grown to 1010 with a median  $\gamma$ -ray flux density of  $6.63 \times 10^{-13}$  photons  $\text{cm}^{-2} \text{MeV}^{-1} \text{s}^{-1}$  and  $\gamma$ -ray spectral index of 2.37. Cross-referencing the catalogs, only 300 unassociated  $\gamma$ -ray sources from 2FGL are represented in 3FGL, which leaves 710 new unassociated  $\gamma$ -ray sources that have a median  $\gamma$ -ray flux density of  $8.96 \times 10^{-13}$  photons  $\text{cm}^{-2} \text{MeV}^{-1} \text{s}^{-1}$  and index of 2.31.

In Section 2 new radio observations are described that have been performed between 2014 and 2015. This is followed by Section 3 where we describe the observational results and provide the complete catalog of radio counterpart candidates for all unassociated 3FGL sources. This is followed by a discussion of the subclass of steady  $\gamma$ -ray emitters in Section 4, which are half of all the detected  $\gamma$ -ray point sources. In Section 4 we discuss the results in the context of understanding the population of unassociated  $\gamma$ -ray sources. Finally in Section 4 we provide a summary and conclusions for our reported findings.

## 2. Observations

The 3FGL catalog covers the entire sky, thus we performed follow-up observations at two radio interferometric arrays: The Australia Telescope Compact Array (ATCA) in the Southern Hemisphere for observing sources with declinations in the range  $[-90^\circ, +10^\circ]$  and the Jansky Very Large Array (VLA) in the Northern Hemisphere for observing sources with declinations  $[0^\circ, +90^\circ]$ . The overlap in sky area was used to cross-check VLA and ATCA calibration procedures. Where a source was detected in both ATCA and VLA data, the VLA results were used.

Combining all observing campaigns with VLA and ATCA, we observed 960 fields around *all Fermi* unassociated sources. We excluded 80 sources for which we had previously found an association from our analysis of radio sources, which fall within the *Fermi* localization error ellipse of 3FGL sources and exhibit parsec-scale emission.

### 2.1. Australia Telescope Compact Array

We have identified 713 objects marked as unassociated in the 3FGL catalog with decl.  $< +10^\circ$ . Together with our previous observations we were able to associate 80 objects with AGNs found to have radio emission on parsec scales using the method described in Petrov et al. (2013) and Schinzel et al. (2015). This is based on the computation of the likelihood ratio between the probability of finding an unrelated background source within the *Fermi* localization error ellipse and the probability of finding a radio counterpart within a given position difference due to random localization errors. The remaining 633 objects were selected as the primary targets for the observations described here. We added 169 secondary targets to the list. These included 122 sources associated on the basis of X-ray emission, 14 sources associated with the low-frequency catalogs NVSS (Condon et al. 1998) and SUMSS (Mauch et al. 2003), and 30 unassociated sources that were in the preliminary version of the 3FGL catalog but not included in the final release. We also included three sources that were marked as unassociated in the preliminary version of the 3FGL but were later associated with pulsars. In total, 805 fields with decl.  $< +10^\circ$  were in the target list.

Observations were made in three campaigns: A3 started on 2014 April 7 and lasted for 30 hr, A4 started on 2014 September 23 and lasted for 66 hr, and A5 started on 2015 April 4 and lasted for 8 hr. Campaign A3 was observed in array configuration H168 with baselines ranging from 61 to 192 m between the inner five antennas and  $\sim 4.4$  km between CA06 and the inner antennas, and campaigns A4 and A5 were observed in H214 configuration with baselines ranging from 92–247 m between the inner five antennas.<sup>7</sup> Observations in all three campaigns were recorded simultaneously in two bands centered at 5.5 and 9.0 GHz with a bandwidth of 2 GHz in both linear polarizations, with circular polarizations derived during processing. The primary flux calibrator was PKS 1934-638. A summary of all observations is listed in Table 1.

A list of 405 target sources were observed in the A3 campaign. In the A4 campaign we observed the remaining 228 primary targets and 172 secondary targets, and we reobserved 303 fields observed in the A3 campaign. There are two reasons for reobservations: (1) we detected a radio source within the  $3\sigma$

<sup>7</sup> [http://www.narrabri.atnf.csiro.au/operations/array\\_configurations/configurations.html](http://www.narrabri.atnf.csiro.au/operations/array_configurations/configurations.html)

**Table 1**  
List of Observations with Connected Interferometers

T	C	Code	Start (UTC)	Dur. (hr)	Tune (GHz)	B/w (GHz)	#	Identifier
ATCA	H214	C2624	2012 Sep 19 10:00	29	5.5/9.0	2.0	411	A1
VLA	A	S5272	2012 Oct 26 11:19	2	5.0/7.3	1.0	41	V1A
VLA	A	S5272	2012 Nov 03 21:01	7	5.0/7.3	1.0	175	V1B
ATCA	H214	C2624	2013 Sep 25 21:30	45	5.5/9.0	2.0	997	A2
ATCA	H168	C2624	2014 Apr 07 16:00	30	5.5/9.0	2.0	405	A3
ATCA	H214	C2624	2014 Sep 23 04:00	66	5.5/9.0	2.0	703	A4
VLA	B	S7104	2015 Mar 16 21:33	1	5.0/7.0	2.0	30	V2A
VLA	B	S7104	2015 Mar 16 22:33	3	5.0/7.0	2.0	107	V2B
VLA	B	S7104	2015 Mar 17 09:46	1	5.0/7.0	2.0	21	V2C
VLA	B	S7104	2015 Mar 21 12:37	4	5.0/7.0	2.0	156	V2D
ATCA	H214	C2624	2015 Apr 04 04:00	8	5.5/9.0	2.0	139	A5
VLA	B	15A-466	2015 Apr 16 20:00	1	5.0/7.0	2.0	19	V2E

**Note.** Column description: T—telescope, C—array configuration, Code—observation proposal code, Start—start time in UTC, Dur.—duration of the observation in hours, Tune—center frequency of the tunings, B/w—bandwidth of each tuning, #—number of targets observed, Identifier—custom observation identifier.

*Fermi* localization error ellipse, but at a distance of more than  $4'$  from the pointing direction—the distance where the primary beam power drops below 20% with respect to the pointing direction at 9 GHz (205 fields); and (2) no source was detected (98 fields). In the latter case we reobserved the field in a seven-element mosaic mode to search for radio counterparts farther from the *Fermi* position, since typically the *Fermi* localization error ellipse is wider than the ATCA field of view. During the A5 campaign we reobserved 13 primary targets that were missed in A4 and six secondary targets that were recorded in only one scan in A4, and we reobserved 120 fields where a source was found at distance of more than  $4'$  from the pointing direction.

Among primary targets 45% of the fields were observed in three scans of 24 s each, 39% were observed in four scans, and 16% were observed in five scans. Among secondary targets, 37% of the sources were observed in two scans; other sources were observed in three or more scans.

The data analysis procedure we used for the A3, A4, and A5 campaigns is described in detail in Petrov et al. (2013). We obtained radio images of size  $1024 \times 1024$  pixels with a pixel size of 2.4 arcsec and a synthesized beam with a typical FWHM size  $20'' \times 30''$ . The majority of sources found look point-like. Two examples of images with extended structure are shown in Figures 1 and 2,<sup>8</sup> though these are the rare exceptions. We determined the flux density of the detected sources, spectral index within a band, and positions. The typical position uncertainty is around  $1''$  and typical uncertainty in flux density is 0.1–0.4 mJy. The detection limit is 1.0–1.5 mJy for sources in the center of the field of view. For sources detected at both 5.5 and 9.0 GHz bands we determined the spectral index across the bands.

Since target sources are observed in two or three scans of 18 s length with a six-element interferometer, the estimates of flux densities of extended objects may have a strong bias and underestimate the peak flux density by up to one order of magnitude. Scrutinizing the data, we found 1%–2% of the reported objects to have questionable estimates of flux density.

<sup>8</sup> Compare the image with [http://cornish.leeds.ac.uk/cgi-bin/public/summary\\_src.py?name=G012.8050-00.2007](http://cornish.leeds.ac.uk/cgi-bin/public/summary_src.py?name=G012.8050-00.2007), [http://atlasgal.mpifr-bonn.mpg.de/cgi-bin/ATLASGAL\\_SEARCH\\_RESULTS.cgi?text\\_field\\_1=G012.8057-0.1994&catalog\\_field=GaussClump](http://atlasgal.mpifr-bonn.mpg.de/cgi-bin/ATLASGAL_SEARCH_RESULTS.cgi?text_field_1=G012.8057-0.1994&catalog_field=GaussClump).

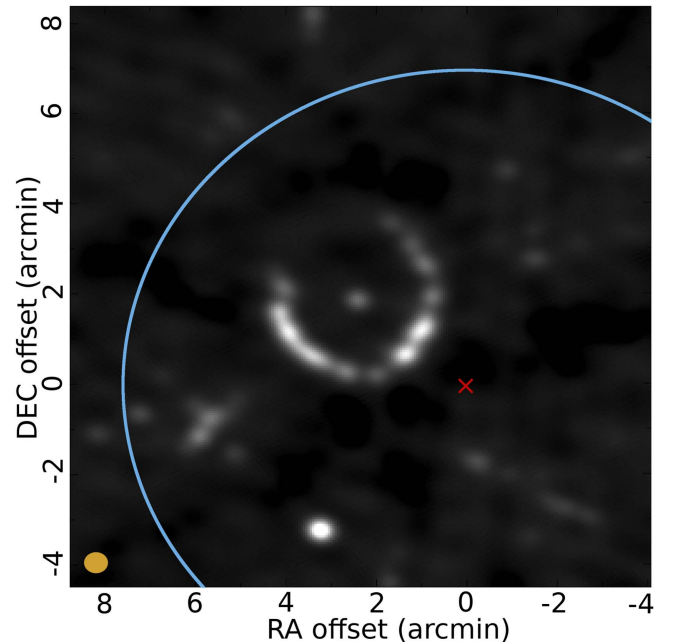


**Figure 1.** Source J1811-1925 located in the heart of the young supernova remnant G11.2–0.3. The position of the sources in the center of the nebula is within  $7''$  of the X-ray pulsar PSR J1811-1925 (Gavriil et al. 2004). The *Fermi* position is shown with a cross and the ellipse marks the edge of the 95% confidence of the  $\gamma$ -ray localization. According to Clark & Stephenson (1977), the remnant is plausibly associated with the historical “guest star” witnessed by Chinese astronomers in the year 386 A.D. The *Fermi* source J1811.3-1927c lies at a distance of  $2.9'$  from the radio source. The bright source south of J1811-1925 is J1811-1930, for which no parsec-scale emission was detected above 6 mJy. The filled circle in the lower left corner indicates the size of the synthesized beam. The image shows 5.5 GHz observed on 2014 September 24 with ATCA. The image rms at the center of the field of view is 2.2 mJy and the peak flux density in this field is 252.7 mJy.

The poor sampling of the Fourier plane as a result of snapshot observations makes it difficult to filter outliers reliably. When in doubt, we tended to keep questionable estimates of flux density, considering it better to keep such problematic estimates than to eliminate a potential candidate for association. Follow-up VLBI observations that are sensitive to the compact components of the objects will filter out Galactic objects that do not have detectable emission on milliarcsecond scales.

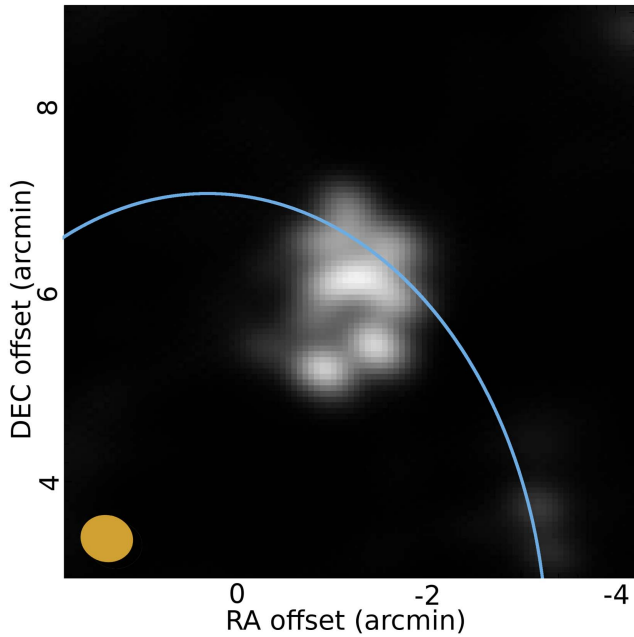


**Figure 2.** Source J1814-1755 in the ultracompact H II region W33, also known as G012.8050-00.2007 in the CORNISH catalog (Urquhart et al. 2013). The nearby  $\gamma$ -ray source is 3FGL J1814.0-1757c. The edge of its 95% confidence localization ellipse is indicated. The filled circle in the lower left corner indicates the size of the synthesized beam. The image shows 5.5 GHz observed on 2014 September 24 with ATCA. The image rms in the center of the field of view is 0.7 mJy and the peak flux density in this field is larger than 40 mJy.

We found a radio object within at least one band and within the area of the  $3\sigma$  *Fermi* localization error ellipse of 497 3FGL unassociated sources out of 633 (79%). For the remaining 21% of the sources no radio counterpart brighter than 2 mJy was found.

## 2.2. Very Large Array

A total of 322 unassociated 3FGL fields with decl. above  $0^\circ$  were selected for observations with NRAO’s Jansky VLA in this campaign (V2). Additionally, we observed the location of 2FGL J0423.4+5612, for which no data were recorded in our previous VLA survey. We reanalyzed our previous campaign V1 (Schinzel et al. 2015) and found that 51 out of 169 (30%) observed fields lie within  $4'$  of 3FGL sources. Among these 51 sources, 18 are marked as associated in 3FGL, and five others were observed in V2. Therefore, combining V1 and V2, we get 491 fields. Of these, 327 are centered at 3FGL sources marked as unassociated, 18 are marked as associated, and 146 are pointed at directions farther than  $4'$  from a 3FGL source.

The observations were conducted using the C-Band receiver covering the frequency range 4–8 GHz, recording a total bandwidth of 4 GHz in both left- and right-handed circular polarizations. The VLA was in B array configuration, thus an integration time of 2 s was chosen. Real-time correlation was performed using VLA’s WIDAR (Wideband Interferometric Digital ARchitecture) correlator. The instantaneous bandwidth was split into two parts, with one half centered at 5.0 GHz (4.0–6.0 GHz) and the other centered at 7.0 GHz (6.0–8.0 GHz). This provides a simultaneous observation of two separate frequency bands. The observing time of 10 hr was split into five segments to be able to observe fields in all ranges of local sidereal time and to increase the likelihood of scheduling (see

Table 1). The first four segments were observed between 2015 March 16 and 21 under time approved through the NASA *Fermi* Guest Investigator program; an additional hour to complete the program was approved as director’s discretionary time and observed on 2015 April 16.

At the beginning of each observing segment either 3C 48 or 3C 286 was observed to provide a bright flux density/bandpass calibrator. In most cases each target source was observed only once with a total integration time of  $\sim 30$  s. Nearby phase calibrators were added with typical integration times of 15 s each in order to solve for changes in the complex gains during the target observations. For all segments the VLA was in B array configuration, providing baseline lengths from 0.21 to 11 km, which results in resolutions of 1 arcsec and a field of view of up to about  $7'$ . The largest angular scale of extended radio structures is about  $29''$ .

The data calibration and analysis procedure is similar to what is described in Schinzel et al. (2015). Major differences were that the newer Common Astronomy Software Applications (CASA) release 4.5.2 and the 31DEC2015 release of the the Astronomical Image Processing System (AIPS; Greisen 1990, pp. 125–142) were used.<sup>9</sup> The data calibration was performed entirely within CASA.

The imaging was performed in CASA using the `clean` task. This task uses a Clark-based clean algorithm (Clark 1980), applies the  $w$ -projection needed for wide-field imaging using 100 projection planes, and visibility weights are determined using the Briggs weighting scheme (Briggs 1995), minimizing sidelobes and noise levels. We used “robust = 0,” which corresponds to a weighting scheme in between uniform and natural. In addition, we used multifrequency synthesis with two terms in order to compensate for spectral changes over the 2 GHz instantaneous bandwidth. This provides both a Stokes I map combining the two polarizations together and a spectral index map. The deconvolution was run with 5000 iterations, a default loop gain of 0.1, and a flux density threshold at which to stop cleaning of 0.06 mJy, corresponding to the approximate thermal noise limit. The primary beam attenuation was corrected using new measurements described in Perley (2016).

All images were then searched using an automatic procedure reading images into AIPS and using the task `SAD` to identify point sources. Custom Python scripts were applied to analyze and inspect the resulting images and point sources found. Sometimes the algorithm applied in `SAD` identifies image artifacts near strong point sources, which were manually flagged in order to retain a clean list of point sources that includes position, flux density, and spectral index for each of the two 2 GHz subbands that are used in subsequent analysis.

## 2.3. VLBI Follow-up Observations

We should stress that estimates of flux densities of emission at kiloparsec scales determined from analysis of ATCA and VLA observations are not sufficient to provide high-confidence associations for *Fermi* sources. First, emission at arcsecond resolutions can have a significant contribution from extended regions of an AGN that often dominate over emission from the AGN’s parsec-scale core. Variability timescales of  $\gamma$ -ray fluxes strongly suggest  $\gamma$ -ray emission to be generated at parsec scales. Second, the number of sources with flux density at

<sup>9</sup> For more information on CASA see <http://casa.nrao.edu/> and for AIPS see <http://www.aips.nrao.edu/index.shtml>.

arcsecond resolution above some limit is significantly greater than the number of sources with flux density above the same limit at milliarcsecond resolutions. Given the large number of weak radio sources located within a typical *Fermi* localization error ellipse at arcsecond resolution, this prevents association of sources weaker than 30–50 mJy. Thus, we suggest that ATCA and VLA observations provide only initial candidates for associations.

Here we report results of our follow-up observations of candidate sources with VLBI. We included 144 target sources detected in ATCA and VLA observations in the ongoing VLBA Calibrator Survey Densification campaign (VCS8/9) at 4.4 and 7.6 GHz (Petrov 2016).<sup>10</sup> The goal of this program is to increase the density of calibrator sources. New AGN candidates for  $\gamma$ -ray association turn out to be good targets for this program. We included a number of target sources in the ongoing LBA Calibrator Survey (LCS-2) at 8.4 GHz, which has similar goals to the VLBA program but is focused on sources in the Southern Hemisphere. The data analysis procedure of the observations is similar to that in previous VCS and LCS campaigns and is described in Petrov et al. (2008, 2011). The detection limit of these programs was in the range 10–12 mJy for sources at elevations above 20° at the telescopes.

We also ran a dedicated VLBA program at 7.6 GHz in 2015 and in 2016 for observing 561 target sources detected by the ATCA and VLA (codes BS241 and S7104) with flux density at 9 GHz exceeding 10 mJy or at 5.5/7 GHz exceeding 20 mJy. Target sources were observed in two scans of four minutes each using a bandwidth of 480 MHz and dual polarization. We ran two LBA experiments in 2014 and 2016 at 8.4 GHz for observing 140 target sources at decl. below  $-40^\circ$ . These target sources were observed in two scans of 210 s each within the spanned bandwidth of 320 MHz. The detection limit for dedicated VLBI observations is 6 mJy when a source is at an elevation above 20° at the telescopes. All VLBI observations were correlated with accumulation periods of 0.1 s and a spectral resolution of 62.5–125 kHz in order to have a wide field of view with sensitivity reduced by no more than 20% within 1' of the pointing direction.

Additional VLBI observations to cover the remaining  $\gamma$ -ray counterparts brighter than 10 mJy in any band are ongoing and will be presented in a future publication.

### 3. Results

#### 3.1. Catalog of Radio Candidates

Similar to Schinzel et al. (2015), we combined the results from the ATCA and VLA observing campaigns into a single uniform data set. This included the results of three ATCA campaigns—A3, A4, and A5—and the VLA campaign V2 that we described in the previous sections, and two further ATCA campaigns and one further VLA campaign. This continues our program of observing unassociated sources in 1FGL and 2FGL catalogs described in our previous publications (Petrov et al. 2013; Schinzel et al. 2015), A1, A2, and V1. We retained 2097 sources—50% of the total number of sources detected—that are within the  $3\sigma$  *Fermi* localization error ellipse and have flux densities above 1 mJy in at least one band. The catalog presented here for the fields observed in the previous A1, A2,

and V1 campaigns is not identical to those previously published and is valid only for 3FGL localizations. First, we reanalyzed the observations. Second, since positions of  $\gamma$ -ray sources in 3FGL and their uncertainties are slightly different than positions in the 1FGL and 2FGL catalogs, some radio sources absent from the published versions are now closer to the 3FGL positions than to 1FGL or 2FGL and are now included, while some radio sources with positions beyond the 3FGL  $3\sigma$  *Fermi* localization error ellipse are now excluded.

If a source was detected at a distance from the pointing direction beyond where the total power drops to 20% of the pointing center, which is 6' 2 at 5 GHz and 4' 2 at 7 GHz, we report only a lower limit on the flux density. The detection limit is 1 mJy at the center of the field of view and 5 mJy at the edge. A number of sources are detected at only one band. This may be due to the source spectrum or because a source was too distant from the pointing direction. We report estimates of spectral index only if a source was detected at both bands within 4' 2 of the pointing direction.

All radio sources found within the  $3\sigma$  *Fermi* localization error ellipse were cross-matched against the reprocessed TIFR GMRT 150 MHz Sky Survey (TGSS) alternative data release 1 (ADR1: Intema et al. 2017), NRAO VLA Sky Survey (NVSS: Condon et al. 1998), Sydney University Molonglo Sky Survey (SUMSS, version 2.1 of 2012 February 16: Bock et al. 1999; Mauch et al. 2003), the Molonglo Galactic Plane Survey 2nd Epoch (MGPS-2: Murphy et al. 2007), the *Gaia* data release 1 (*Gaia*: *Gaia* Collaboration et al. 2016), and the *Wide-field Infrared Survey Explorer* (*WISE*) catalog<sup>11</sup> (ALLWISE, 2013 November 13: Wright et al. 2010; Mainzer et al. 2011), which combines the data from the *WISE* cryogenic and post-cryogenic survey phases and provides the most comprehensive view of the full mid-infrared sky currently available. We obtained 837 matches with the ALLWISE catalog, 1291 matches with the *Gaia* DR1 catalog, 1051 matches with NVSS, 461 matches with SUMSS and MGPS-2, and 507 matches with TGSS ADR1. We evaluated the probability of a false detection for *Gaia* counterparts in the following way. We counted the number of sources in a uniform  $0.25 \times 0.25$  grid and converted it to the density of *Gaia* sources per steradian. We then defined the probability of false detection as the product of the area in the search radius and the local density of *Gaia* sources (Petrov & Kovalev 2017). The search radius is 0' 2 for sources associated with VLBI, and 3' 0 otherwise. A search radius of 0' 2 for VLBI-associated sources was selected to accommodate possible position errors in *Gaia*.

Table 2 presents the catalog of detected sources within  $3\sigma$  of the *Fermi* localization error ellipse. The table of the remaining 1842 sources detected outside the  $3\sigma$  *Fermi* localization error ellipse can be found in the tar.gz package attachment.

#### 3.2. New Associations

In order to establish the association of a parsec-scale source with its  $\gamma$ -ray counterpart we run a likelihood ratio test using Poisson statistics. The likelihood ratio of association  $\Lambda$  is defined as ratio of the probability that the  $\gamma$ -ray and radio source founds at separation  $d$  are physically the same object, and their difference in position is due to statistical errors only, to the probability that the radio source is a background,

<sup>10</sup> <http://astrogeo.org/vcs9>

<sup>11</sup> <http://wise2.ipac.caltech.edu/docs/release/allwise/>

**Table 2**  
First Eight Rows of 2097 Objects Found within the  $3\sigma$  *Fermi* Localization Error Ellipse

(1)	(2)	(3)	(4)	(5)	(6)	(7)	(8)	(9)	(10)	(11)	(12)	(13)	(14)	(15)	(16)	(17)	(18)	(19)	(20)	(21)	(22)
FRC J0000 +6309	00 00 19.26	+63 09 51.96	0.30	0.30		14.8	0.1						V2	3FGL J0001.0 +6314	6.68	1.73					
FRC J0000 +6315	00 00 17.36	+63 15 35.93	0.30	0.30		1.3	0.1						V2	3FGL J0001.0 +6314	4.98	1.35					
FRC J0000- 3738	00 00 08.39	-37 38 19.95	0.90	0.85		17.4	0.1		17.6	0.2	0.02	0.03	A3	3FGL J0000.2- 3738	1.36	0.86	RFC J0000- 3738	22.0	206.5	SUMSS J000008- 373819	18
FRC J0001 +3524	00 01 38.83	+35 24 31.24	0.30	0.30				>	3.7	0.1			V2	3FGL J0001.6 +3535	10.92	2.24					
FRC J0001- 4155	00 01 32.72	-41 55 25.41	0.80	0.80		9.5	0.1		12.0	0.3	0.47	0.07	A4	3FGL J0002.2- 4152	8.24	2.52	RFC J0001- 4155	9.0	1.3	SUMSS J000133- 415524	13
FRC J0002 +6219	00 02 53.52	+62 19 17.04	0.30	0.30		3.5	0.2		1.8	0.2	-1.76	0.44	V1	3FGL J0002.6 +6218	1.84	1.45					
FRC J0002- 6716	00 02 28.13	-67 16 11.57	0.80	0.80		4.9	0.1		4.2	0.1	-0.31	0.09	A4	3FGL J0002.0- 6722	6.38	2.96				SUMSS J000228- 671612	32
FRC J0002- 6726	00 02 15.19	-67 26 53.41	0.80	0.80		11.2	0.1		14.8	0.1	0.57	0.03	A4	3FGL J0002.0- 6722	4.78	2.13	RFC J0002- 6726			SUMSS J000215- 672652	19
(23)	(24)	(25)	(26)	(27)	(28)	(29)	(30)	(31)	(32)	(33)											
NVSS 000019+630951	18.9			WISE J000019.04+630952.9	15.72																
NVSS 000017+631538	3.0			WISE J000017.42+631535.5	14.29	GAIA 430090779421378688	19.98	00 00 17.28832	+63 15 38.4358	0.00076											
NVSS 000008-373819	15.4			WISE J000008.41-373820.6	14.57																
NVSS 000138+352432	10.9			WISE J000138.71+352430.1	15.93																
				WISE J000132.74-415525.2	13.99	GAIA 4995979729065629312	18.40	00 01 32.75326	-41 55 25.3234	0.00018											
NVSS 000253+621917	12.7	TGSS J000253.2+621917	140.4	WISE J000253.17+621917.6	14.19	GAIA 429932308004616192	17.23	00 02 53.22260	+62 19 18.0223	0.00003											
				WISE J000228.45-671608.7	14.60																
				WISE J000215.19-672653.4	14.51	GAIA 4707413417751868800	18.21	00 02 15.18729	-67 26 53.4893	0.00005											

**Note.** Column descriptions: (1) IAU name; (2), (3) R.A. and decl.; (4), (5) uncertainties in R.A. without  $\cos \delta$  factor; (6)–(8) flux density flag, flux density estimate at the low-frequency band, and its uncertainty in mJy; (9)–(11) flux density flag, flux density estimate, and its uncertainty at the high-frequency band 7/9 GHz; (12), (13) spectral index defined as  $S \sim \nu^{\alpha}$  between low- and high-frequency bands; (14) campaign code; (15) 3FGL source name; (16) distance between the radio sources and the  $\gamma$ -ray source position in arcmin; (17) the same distance divided by  $1\sigma$  *Fermi* position uncertainty; (18)–(20) name of a counterpart in the VLBI catalog RFC (available at <http://astrogeo.org/rfc>) (L. Petrov & Y. Y. Kovalev 2017, in preparation) within  $20''$ , the correlated flux density at 8 GHz in mJy, and the likelihood ratio (as described in Section 3.2) of radio- $\gamma$ -ray association; (21), (22) name of a counterpart from SUMSS or MGPS-2 catalogs found within  $40''$  and its flux density in mJy; (23), (24) name of a counterpart from the NVSS catalog found within  $20''$  and its flux density in mJy; (25), (26) name of a counterpart from the TGSS catalog and flux density at 150 MHz; (27), (28) name of a counterpart from the ALLWISE catalog found within  $3''$  and its magnitude at wavelength  $3.4 \mu\text{m}$ ; (29), (30) ID of a counterpart from the optical *Gaia* DR1 catalog found within  $0''.2$  for sources associated with VLBI and  $3''.0$  otherwise and its magnitude at filters G; (31), (32) *Gaia* position; (33) the probability of false association with *Gaia*. If the flux density flag in (6) or (9) is “<,” that means the source was detected with a sidelobe and the reported flux density is the lower limit.

(This table is available in its entirety in machine-readable form.)

unrelated object. Simple geometric consideration results in

$$\Lambda = \frac{e^{-n^2/2}}{N(1)S^p d^2/4}, \quad (1)$$

where  $d$  is the angular separation in radians between the radio and  $\gamma$ -ray positions,  $S$  is the radio flux density in jansky,  $n$  is the normalized distance between the radio and  $\gamma$ -ray sources<sup>12</sup>,  $N(1) = 374$ , and  $p = -1.2088$ . The numerical values were determined from the  $\log N$ – $\log S$  relation of correlated flux densities. Detailed descriptions for determining the probabilities of association and the numerical value of the  $\log N$ – $\log S$  diagram are given in Petrov et al. (2013) and Schinzel et al. (2015).

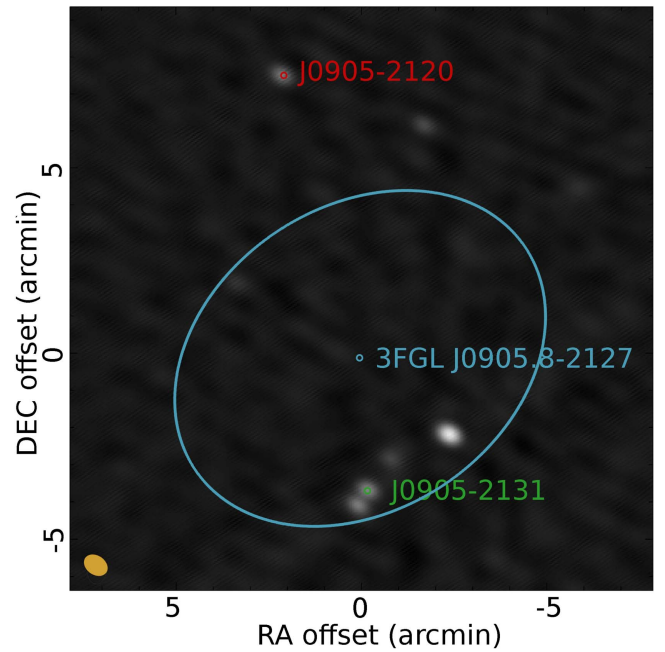
In total, we performed VLBA or LBA observations in the fields that contain 798 sources detected in our VLA and ATCA programs within  $1'$  of the pointing direction. We employed such a wide field of view because a compact source with emission at parsec scales is not always coincident with the peak brightness of the radio structure on kiloparsec scales. Petrov (2013) demonstrated a number of such examples.

We have detected 451 compact sources from these VLBI observations. Among 2097 sources detected in our ATCA and VLA programs, there are 744 objects with flux densities greater than 10 mJy at either 5.5 or 9 GHz. Of these, 630, or 85%, have been followed up with VLBI. The remaining 114 objects, primarily in the Southern Hemisphere, will be observed in the near future.

We have computed the likelihood ratio among 451 VLBI sources detected within  $1'$  of objects observed in VLA and ATCA programs. We consider the sources with  $\Lambda > 8$  and a normalized arc length of  $n < 3$  as associations. The probability that the normalized arc length exceeds 3 due to random errors in the  $\gamma$ -ray source position is 1.1%. That means that by setting this criterion we will have false negative associations for 1% of the sources. We selected the  $\Lambda > 8$  criterion to have approximately the same number of false positive associations. In total, we have 19 double VLBI associations for 1530  $\gamma$ -ray sources. Excluding the two gravitational lenses 3FGL J0221.1+3556 and 3FGL J1833.6-2103, we get a false positive probability of 1.1%. We performed an additional test: we rotated the VLBI catalog at random angles in the range  $[0^\circ, 100^\circ]$ , ran 256 test associations, and found an average of 18.9 associations. Thus, we conclude that the probability of false association of this criterion, both positive and negative, is around 1%.

We found that 286 sources out of 451 (63%) have—and therefore are listed as—associations based on their parsec-scale emission. Of these, 144 have associations reported in the 3FGL catalog. Of those, three *Fermi* sources have two associations. Association based on parsec-scale emission confirms them and allows us to improve their positional accuracy to milliarcsecond scales. We have further established new associations with AGNs for 142 sources. Of these, two *Fermi* sources have two associations.

In the majority of fields observed with ATCA and VLA we found more than one point source that is a candidate for association. VLBI observations allow us to find which of these point sources have parsec-scale detectable emission and therefore identify the likely counterpart. Figure 3 provides an



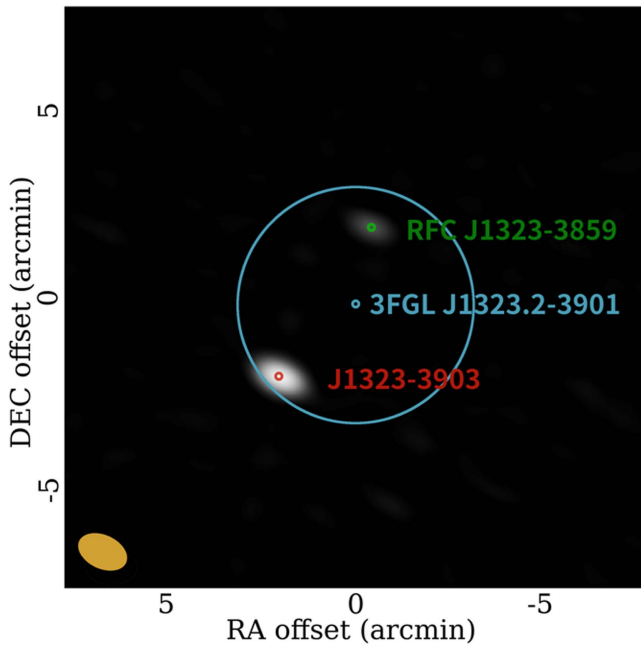
**Figure 3.** The field observed with ATCA at 5.5 GHz centered on 3FGL J0905.8-2127. Among six point-like sources seen in the field, two have been detected with the VLBA at 7.6 and 4.4 GHz. Source J0905-2131 has a likelihood ratio of 22.9, which is above the threshold for establishing association based on parsec-scale emission. The filled circle in the lower left corner indicates the size of the synthesized beam. The image shows 5.5 GHz observed on 2014 April 8 with ATCA. The image rms in the center of the field of view is 0.2 mJy and the peak flux density is 21.9 mJy.

illustration of this. There are six point sources in the field. Of these, two show parsec-scale emission at a level  $>20$  mJy. The first, J0905-2120, has a  $\Lambda$  of 2.5, which is below the threshold of 8 for a reliable association, and the second, J0905-2131, which is a double at  $28''$ , has a  $\Lambda$  of 22.9, and thus we considered it to be associated with the 3FGL object J0905.8-2127. Figure 4 illustrates another situation. There are two sources detected with ATCA  $4' 7''$  apart within the 3FGL J1323.2-3901 localization error ellipse: J1323-3859 and J1323-3903. The first source has a flux density of 6.3 mJy at 5.5 GHz and a spectral index of  $+0.5$ , while the second one has flux density of 29.0 mJy and a spectral index of  $-0.8$ . One may expect that the stronger source is a probable association. However, VLBI observations revealed compact emission from the weaker source J1323-3859 and no compact emission from J1323-3903.<sup>13</sup>

Finally, we present Table 3, which provides the list of our proposed 291 associations based on parsec-scale emission at 8 GHz detected with follow-up VLBI of point sources found in our ATCA and VLA observations. We note that association of J1413-6520 in this list is problematic. The ATCA observations provide the position of the Circinus galaxy, while with

<sup>12</sup> The distance between the radio and  $\gamma$ -ray localizations divided by the  $1\sigma$  *Fermi* localization error.

<sup>13</sup> It is interesting that the VLBI flux density of J1323-3903 at 8 GHz, 23 mJy at epoch 2015.02.24 and 31 mJy at epoch 2015.11.10, is significantly higher than its ATCA flux density of 8 mJy at 9 GHz at epoch 2014.04.07. The flux density of J1323-3903 found in the same field extrapolated to 1.4 GHz is  $89 \pm 6$  mJy, which is rather close to the value from NVSS of 70 mJy. The flux density of J1323-3859 extrapolated to 1.4 GHz would be  $3.1 \pm 0.4$  mJy, and it was not detected in the NVSS with a limit of 2.4 mJy. These comparisons with NVSS demonstrate that there is no gross oversight in the ATCA data calibration. Therefore, we attribute the discrepancy between ATCA and VLBI estimates of flux density to source variability.



**Figure 4.** The field observed with ATCA at 5.5 GHz centered on 3FGL J1323.2-3901. ATCA observations identified two sources, J1323-3859 and J1323-3903 as candidates for association. VLBI follow-up observations at 8 GHz revealed compact emission only from the weaker source J1323-3859, and thus discriminated against the other candidate. The filled circle in the lower left corner indicates the size of the synthesized beam. The image shows 5.5 GHz observed on 2014 April 24 with ATCA. The image rms in the center of the field of view is 0.1 mJy and the peak flux density is 29.0 mJy.

VLBI we detected only emission from the supernova remnant 1996cr,  $20''.86$  away.

### 3.3. Previously Reported 3FGL Associations

Among 170 sources with associations reported by the 3FGL team we overturned five associations for radio sources that are AGNs and provide alternative associations for two pulsars (see Table 4). For all five AGNs we suggest new associations that are closer to the 3FGL position than the associations suggested by the *Fermi* team. Laffon et al. (2015) report  $\gamma$ -ray pulsation with the same period as millisecond pulsar PSR J0931-19. The pulsar PSR J0931-19 and the AGN RFC J0930-1903 are two different objects. One explanation of why two methods—detection of parsec-scale emission and detection of radio pulses—led to different sources is that errors in *Fermi* localization of 3FGL J0930.9-1904 may be larger than their formal uncertainties.

We have detected radio counterparts within  $1'$  of all 122 observed X-ray sources associated with *Fermi* sources. The median difference in position between ATCA and X-ray positions is  $6''.8$ , with seven objects detected at distances in the range  $30''$ – $51''$ . ATCA observations provided improvement in positions for 85% of the sources. We observed 84 out of 122 sources with the VLBA and detected 82. Among the remaining 38 objects, 28 have a flux density from ATCA observations above 10 mJy. They will be observed with VLBI in the future.

On the basis on these observations, we can conclude that association of 3FGL sources based on the X-ray emission matches very well with association based on radio emission from parsec scales. We strongly confirmed two out of three X-ray associations, and found no X-ray sources from our

sample of 122 objects that have not been detected at 5.5 or 9 GHz.

### 3.4. Extended Sources

All target fields observed with ATCA and VLA were imaged and visually inspected. We found 158 fields where sources showed emission larger than the synthesized beam. Two classes of such extended sources were identified: large angular structures (LASs) that were either resolved or over-resolved, and double sources or point sources with extensions. Table 5 lists the 3FGL source in those fields and their corresponding localization within that field, distance to the 3FGL position, and structural classification.

Most sources found either exhibit a shell-like structure, as shown in Figures 1, 6, and 8, or show a morphology that resembles double-lobed sources or one-sided jets, as in Figures 5 and 7. In 36 cases an extended source was found within the  $2\sigma$  *Fermi* localization error ellipse, of which 19 were classified as LASs and 17 as double sources. Figure 9 shows the sky distribution of the extended sources. From this plot it is evident that LAS sources are primarily located within the Galactic plane, whereas double sources are primarily found outside the Galactic plane. Judging from the morphologies and radio spectral properties of the objects shown in Figures 6 and 8, we see that they resemble supernova remnant shells or H II regions.

1. In the case of 3FGL J2004.4+3338 the shell is found within the  $1\sigma$  localization of the  $\gamma$ -ray source and is most likely associated with it. An infrared counterpart is found for this structure in the ALLWISE catalog (Wright et al. 2010; Mainzer et al. 2011), J200423.63+333904.2.
2. In the case of 3FGL J0225.8+6159 the shells are found more than  $5\sigma$  away from the  $\gamma$ -ray localization. This object also has an infrared (IR) counterpart in the ALLWISE catalog, J022537.37+620553.3. This indicates the presence of an H II region in both cases.
3. The case of Figure 5 shows an extended steep-spectrum radio source that could be a compact symmetric object (CSO) (Wilkinson et al. 1994; Readhead et al. 1996), but more likely is a radio galaxy, due to the lack of evidence for the presence of a single compact core. Higher resolution observations are required to understand the nature of this object. It is found within the  $2\sigma$  localization of 3FGL J0154.1+4642.
4. Figure 7 shows an example of two extended sources separated by  $\sim 8''$ . Both of these have a steep spectral index, and if related they resemble the structure of a radio galaxy. In this case this structure is located within  $1\sigma$  of the  $\gamma$ -ray localization.

Overall, the source classes defined above seem to separate a Galactic population of extended radio sources and an extragalactic one.

### 3.5. Empty Fields

The list of 245 3FGL sources with no radio counterpart brighter than 2 mJy at 5 GHz within the  $3\sigma$  *Fermi* localization error ellipse is presented in Table 6. Of these, 237 are marked as unassociated in the 3FGL catalog, four are associated with pulsars, and one is associated with NVSS J224604+154437. The latter association was not confirmed. The remaining three

**Table 3**

First Eight Rows of the List of 291 Associations of 3FGL Objects that have a Likelihood Ratio of their Association of More than 8 Based on their Parsec-scale Radio Emission Detected with Follow-up VLBI Observations

3FGL Name	VLBI Name	R.A. (h m s)	Decl. ( $^{\circ}$ ' ")	$\sigma_{\alpha}$ (mas)	$\sigma_{\delta}$ (mas)	Corr.	$D$ ( $^{\circ}$ )	$N\sigma$	$S$ (mJy)	$\Lambda$	3FGL ass.
3FGL J0000.2–3738	RFC J0000–3738	00 00 08.414182	–37 38 20.67354	0.54	1.10	0.178	1.36	0.86	22.0	207.2	
3FGL J0003.2–5246	RFC J0003–5247	00 03 19.600260	–52 47 27.28128	19.44	10.13	–0.272	1.04	0.70	15.0	194.3	RBS 0006
3FGL J0006.2+0135	RFC J0006+0136	00 06 26.924724	+01 36 10.38555	1.07	2.16	–0.413	2.64	1.48	14.0	33.0	
3FGL J0007.4+1742	RFC J0007+1745	00 07 18.873920	+17 45 34.56806	0.16	0.26	–0.201	3.72	0.84	22.0	28.2	
3FGL J0007.9+4006	RFC J0007+4008	00 07 41.666525	+40 08 29.93735	0.42	0.66	0.258	3.43	1.19	14.0	20.1	
3FGL J0008.3+1456	RFC J0008+1456	00 08 25.399845	+14 56 35.79096	0.18	0.32	–0.049	1.19	0.40	21.0	104.5	
3FGL J0008.6–2340	RFC J0008–233A	00 08 35.399660	–23 39 28.00793	0.32	0.80	0.133	1.70	1.09	29.0	202.1	RBS 0016
3FGL J0010.5–1425	RFC J0010–1420	00 10 41.940201	–14 20 20.33807	0.26	0.56	–0.149	5.49	1.24	21.0	8.4	

**Note.** Column description: 3FGL Name—3FGL identifying name; VLBI Name—IAU name; R.A./decl.—J2000 coordinates of VLBI detection;  $\sigma_{\alpha}$ —uncertainty in R.A. without  $\cos \delta$  factor in mas;  $\sigma_{\delta}$ —uncertainty in decl. in mas; Corr.—correlation between R.A. and decl. estimates;  $D$ —separation between radio and  $\gamma$ -ray sources in arcminutes;  $N$ —normalized separation between radio and  $\gamma$ -ray sources;  $S$ —total VLBI flux density at 8 GHz integrated over the images in mJy;  $\Lambda$ —likelihood ratio; 3FGL ass.—3FGL association.

(This table is available in its entirety in machine-readable form.)

**Table 4**

Objects with Alternative Associations Based on Parsec-scale Emission

3FGL Name	Type	Old Association	Suggested Association
3FGL J2021.9+0630	AGN	87 GB 201926.8 +061922	RFC J2021+0629
3FGL J0332.0+6308	AGN	GB6 J0331+6307	RFC J0331+6308
3FGL J0150.5–5447	AGN	PMN J0150–5450	RFC J0150–5450
3FGL J0415.7–4351	AGN	SUMSS J041605 –435516	RFC J0416–4350
3FGL J1838.5–6006	AGN	SUMSS J183806 –600033	RFC J1838–6005
3FGL J0930.9–1904	pulsar	PSR J0931–19	RFC J0930–1903
3FGL J2017.6–1616	pulsar	PSR J2017–1618	RFC J2017–1618

are associated with supernova remnants (SNRs), namely 3C 391, MSH 17-39, and 3CTB 37A. Among those 245 “empty” fields we found evidence for extended radio emission in 39 cases listed in Table 5. In those cases there is evidence for extended emission with a total flux density of  $>2$  mJy, but no individual bright spots exceed  $>2$  mJy. This leaves 206 empty fields in which we did not detect a radio source above 2 mJy with the VLA or ATCA. We call these fields “empty” in the sense that there are no radio sources brighter than 2 mJy within the observed frequency range. As Frail et al. (2016) noted, some of these fields contain weak objects listed in low-frequency NVSS and SUMSS catalogs. The locations of the empty fields on the sky are illustrated in Figure 9, which shows no apparent concentration of empty fields in the Galactic plane.

**Table 5**First Eight Rows of 158 Extended Sources Found in Radio Observations Targeting 3FGL Unassociated  $\gamma$ -Ray Objects

3FGL Name	R.A. (h m s)	Decl. ( $^{\circ}$ ' ")	$D$ ( $^{\circ}$ )	Nd	C
J0000.1+6545	23 59 41.68	+65 42 3.456	4.14	3.3	2
J0003.2–5246	00 03 11.60	–52 41 37.20	5.04	5.5	2
J0003.4+3100	00 03 20.13	+30 55 25.01	5.24	2.1	1
J0020.9+0323	00 20 50.30	+03 23 43.10	1.29	1.6	2
J0026.2–4812	00 25 37.47	–48 16 39.11	7.27	4.5	2
J0154.1+4642	01 53 56.09	+46 38 51.47	3.89	1.7	1
J0225.8+6159	02 25 37.82	+62 05 53.76	6.92	5.8	1
J0026.2–4812	00 25 53.27	–48 16 43.19	5.34	3.3	2

**Note.** Column description: 3FGL Name—object identifier, R.A./Decl.—coordinates,  $D$ —distance from  $\gamma$ -ray localization, Nd— $\sigma$  from  $\gamma$ -ray localization, C—Extended source class: 1—large angular scale object; 2—double or jetted source.

(This table is available in its entirety in machine-readable form.)

However, counting the number of empty fields, 27% (65/245) lie within  $1^{\circ}$  of the Galactic plane. There were 54 matches of TGSS ADR1 sources (Intema et al. 2017) that were found within  $3\sigma$  of the  $\gamma$ -ray localization. Such sources are most likely steep-spectrum radio sources and are good candidates for pulsar searches.

Notable are 95/245 (39%) empty fields that are found  $\pm 10^{\circ}$  outside the Galactic plane. Their median  $\gamma$ -ray flux density is  $5.96 \times 10^{-13}$  photons  $\text{cm}^{-2} \text{s}^{-1} \text{MeV}^{-1}$  and their median  $\gamma$ -ray spectral index is 2.4. Their median variability index is 47.0 (Ackermann et al. 2011), which indicates that most of the sources can be assumed to be nonvariable. The spectral index corresponds to the median of the total population of  $\gamma$ -ray point sources.

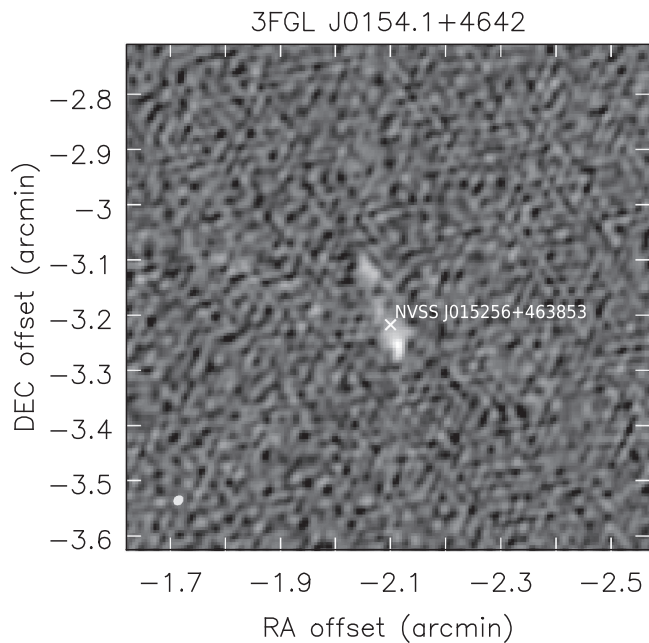


**Figure 5.** This extended source was found in the field of 3FGL J0154.1+4642 observed with the VLA on 2015 March 16. The coordinates are shown relative to the centroid of the  $\gamma$ -ray localization, with the field shown lying inside the 68% and 95% confidence areas of the localization. The peak flux in the 5.0 GHz map is  $0.6 \text{ mJy beam}^{-1}$ , the integrated flux density is  $4.6 \text{ mJy}$ , and the image rms at the center of the field of view is  $58 \mu\text{Jy beam}^{-1}$ . The in-band spectral index at the peak value is  $-2.31 \pm 0.69$ . The position of NVSS J015356+463853 is marked with an “x” in the field. The filled circle in the lower left corner indicates the size of the synthesized beam.

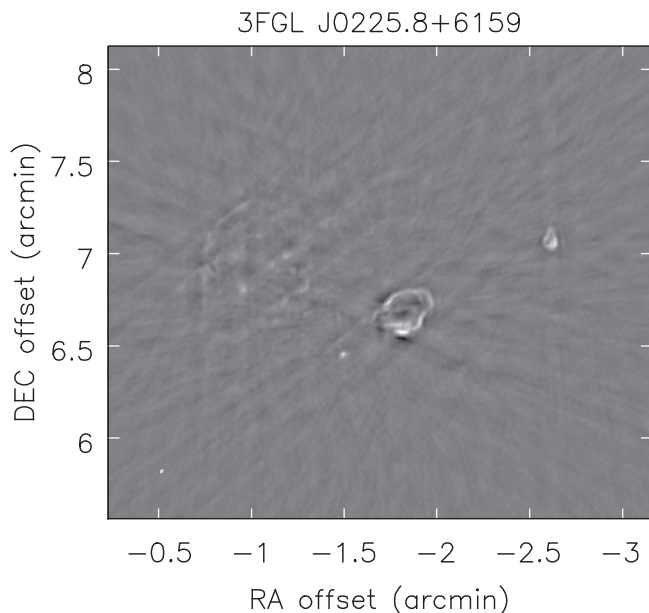


**Figure 6.** These extended sources were found in the field of 3FGL J0225.8+6159 observed with the VLA on 2015 March 16. The coordinates are shown relative to the centroid of the  $\gamma$ -ray localization, with the field shown lying far outside the 95% confidence region of the localization. The peak flux of the central source shown in the 5.0 GHz map is  $6.3 \text{ mJy beam}^{-1}$ , the integrated flux density is  $50.0 \text{ mJy}$ , and the image rms at the center of the field of view is  $0.1 \text{ mJy beam}^{-1}$ . The peak flux density of the northwest source is  $5.1 \text{ mJy beam}^{-1}$  with a flux density of  $30.7 \text{ mJy}$ . The in-band spectral index for both is  $-4 \pm 1$ . The filled circle in the lower left corner indicates the size of the synthesized beam.

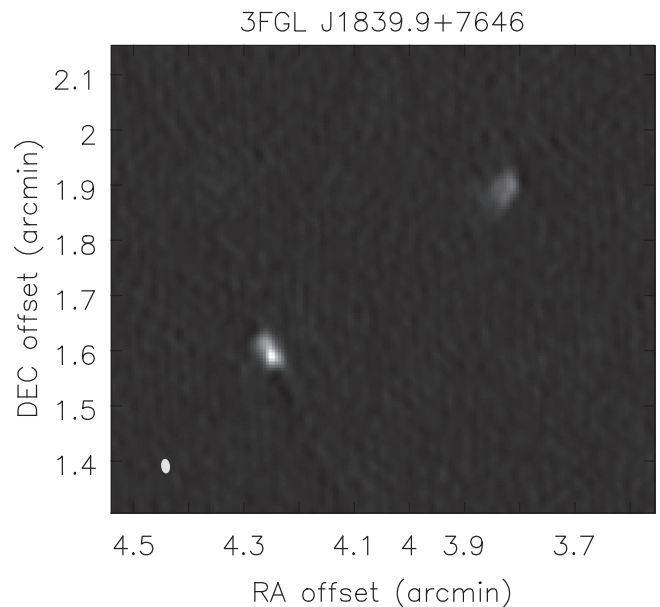


**Figure 7.** This extended source was found in the field of 3FGL J1839.9+7646 with the VLA at 5.0 GHz observed on 2015 March 16. The coordinates are shown relative to the center of the  $\gamma$ -ray localization, with the field shown lying inside the 68% and 95% confidence areas of the localization. The in-band spectral index of the southeast source is  $-2.5 \pm 0.1$  and that of the northwest source is  $-1.9 \pm 0.2$ . The peak flux in the map is  $6.2 \text{ mJy beam}^{-1}$ , the integrated flux density over both sources is  $26.6 \text{ mJy}$ , and the image rms at the center of the field of view is  $65 \mu\text{Jy beam}^{-1}$ . The filled circle in the lower left corner indicates the size of the synthesized beam.

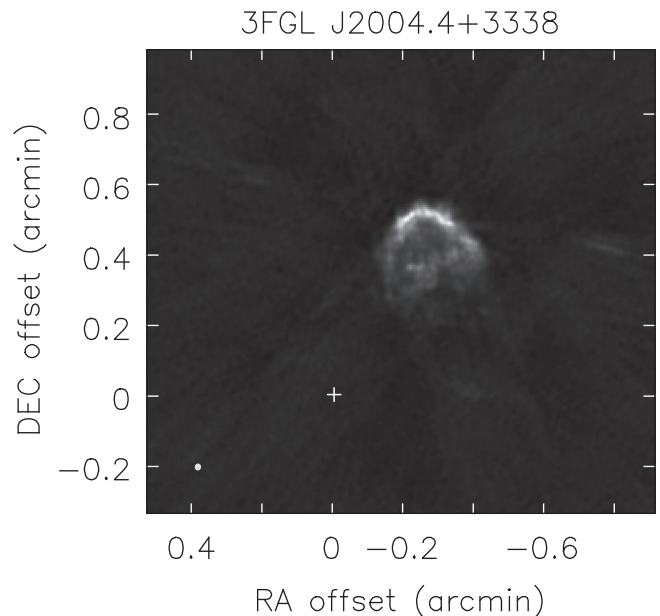


**Figure 8.** This shell-like structure was found with the VLA at 5.0 GHz in the field near 3FGL J2004.4+3338 observed on 2015 March 16. The coordinates are shown relative to the centroid of the  $\gamma$ -ray localization, which is marked with a cross. The object lies within the 68% and 95% confidence regions of the  $\gamma$ -ray source. It has an in-band spectral index of  $-0.9 \pm 0.3$ , an integrated flux density of  $247 \text{ mJy}$ , a peak flux of  $4.2 \text{ mJy beam}^{-1}$ , and an image rms at the center of the field of view of  $70 \mu\text{Jy beam}^{-1}$ . The filled circle in the lower left corner indicates the size of the synthesized beam.

#### 4. Discussion and Summary

With the newer *Fermi*/LAT catalogs providing longer averaging time, one can see that from 2FGL to 3FGL the

**Table 6**

First Eight Rows of the List of 245 3FGL Unassociated Objects that have No Radio Source Brighter 2 mJy within the  $3\sigma$  *Fermi* Localization Error Ellipse

3FGL	TGSS ADR1	$D$ ( $^{\circ}$ )	Nd
3FGL J0001.6+3535	J000051.8+352741	12.0	150.6
3FGL J0003.5+5721	J000332.3+572711	05.6	167.9
3FGL J0004.2+6757	...	...	...
3FGL J0017.1+1445	...	...	...
3FGL J0022.7+4651	J002212.5+464402	09.0	122.5
3FGL J0032.5+3912	...	...	...
3FGL J0039.3+6256	...	...	...
3FGL J0051.6+6445	...	...	...

**Note.** In the 98 cases where a TGSS ADR1 was found within the  $3\sigma$  *Fermi* localization error ellipse, the corresponding identifier, separation, and  $\sigma$  are listed. Column descriptions: 3FGL—3FGL catalog source name; TGSS ADR1—TGSS ADR1 source name (Intema et al. 2017);  $D$ —angular distance in arcmin between  $\gamma$ -ray and TGSS ADR1 localizations; Nd—normalized angular distance between  $\gamma$ -ray and TGSS ADR1 localizations.

(This table is available in its entirety in machine-readable form.)

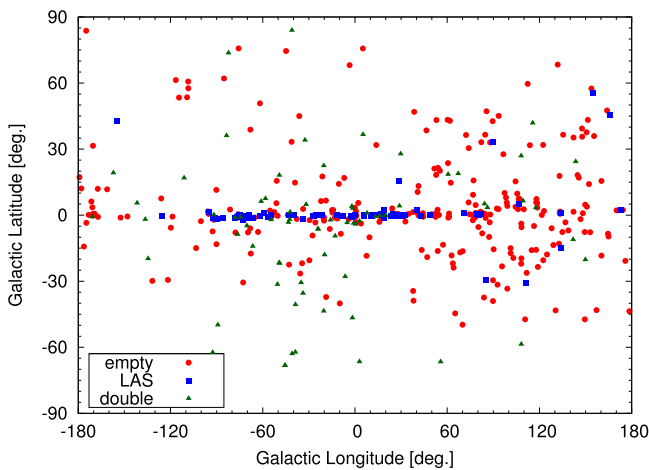


**Figure 9.** Sky distribution in Galactic coordinates of empty fields, large angular size sources, and fields with double or extended point sources.

median fluxes of unassociated  $\gamma$ -ray sources have dropped by a factor of 1.8. Since these two catalogs were derived using different diffuse background models and slightly different methods, we use only values from 3FGL in the following analysis, and when referring to 2FGL sources the values of the 300 cross-listed objects are chosen. Comparing the group of previously found unassociated  $\gamma$ -ray sources with the group of newly found ones and using the 3FGL reported variability indices, we find that 3.0% of previously reported objects are variable compared to 2.4% of newly found objects. This shows that the majority of unassociated  $\gamma$ -ray sources do not show significant  $\gamma$ -ray variability and could be considered steady  $\gamma$ -ray emitters. Since most of the unassociated sources are steady emitters this cannot be used to distinguish different populations such as fields associated with AGNs or empty fields. An additional complication arises from the fact that finding variability in fainter  $\gamma$ -ray sources is very difficult given the poor photon statistics.

Despite pushing toward lower  $\gamma$ -ray flux densities in the newest  $\gamma$ -ray source catalogs, we continue to increase the number of AGN associations using radio observations. Eventually, this will lead to a reduction in the completeness

limit of the radio flux density of  $\gamma$ -ray radio counterparts by a factor of 10, from 100 mJy to around 10 mJy. With the results presented here, together with previous observations, we have firmly associated 144 new  $\gamma$ -ray objects with newly discovered AGNs and improved positions of 170 previously associated sources to the milliarcsecond level of accuracy. We expect to increase this number after all VLBI follow-up observations have been completed. This marks the single largest reduction in unassociated sources by any follow-up program to date and demonstrates the strength of this effort in comparison to relying solely on the analysis of existing multiwavelength catalogs. In the global context this corresponds to a reduction in 3FGL unassociated sources by 14%, leaving 901 sources without a multiwavelength counterpart. Note that the total number of known  $\gamma$ -ray pulsars is currently 220<sup>14</sup>, against 1550  $\gamma$ -ray AGNs with radio emission from parsec scales. A recent publication discussing potential new  $\gamma$ -ray pulsar candidates highlights the challenges involved in finding more  $\gamma$ -ray pulsars (Frail et al. 2016).

The most remarkable results presented here are the so-called empty fields, which are not necessarily empty, but for which no radio point source brighter than several mJy was found in the region of the  $\gamma$ -ray localization. We first pointed these fields out in Schinzel et al. (2015). For 2FGL unassociated sources those empty fields were primarily localized within the Galactic plane. However, 39% of empty fields were found outside the Galactic plane. This hints at an extragalactic distribution in addition to the previously found Galactic one. There is still a possibility that a large number of empty fields are related to pulsars, which are also found outside the Galactic plane. However, another possibility could be the presence of radio-quiet AGNs that are not found in optical/IR catalogs. It is expected that high-frequency peaked AGNs have very faint radio flux densities, due to the shifting of their overall spectral energy distribution to higher energies.

We found extended radio sources in at least 16% (154) of observed radio fields, and 36 of these sources lie within  $2\sigma$  of the  $\gamma$ -ray source. These extended sources were broken down into two subclasses, one indicating an LAS object and the second indicating the presence of a double or jet-like extended source. The first subclass could be related to Galactic SNRs or H II regions, which should be further investigated with more compact interferometer configurations or radio observations at lower frequencies, as well as a systematic comparison to infrared observations, which could distinguish the SNR origin from H II regions. The majority of sources found in the second subclass are most likely radio galaxies, but could also contain CSOs. High-resolution VLBI spectral imaging observations are needed to determine the nature of those objects, which has been done in the case of 2234 + 282 (An et al. 2016). However, no convincing CSO  $\gamma$ -ray emitter has been found to date at redshifts beyond  $z > 0.006$ . Establishing a firm association of a CSO or distant radio galaxy with a  $\gamma$ -ray source would challenge existing interpretations of the physics of the production of  $\gamma$ -ray emission.

In summary, we present an update of our work on new associations for  $\gamma$ -ray unassociated sources found by *Fermi*. For all 3FGL unassociated sources we performed radio observations with compact interferometers, which provided 2097 radio objects as candidates for association. We have

<sup>14</sup> <https://confluence.slac.stanford.edu/display/GLAMCOG/Public+List+of+LAT-Detected+Gamma-Ray+Pulsars>

observed a large fraction of those and provided milliarcsecond-scale detections. For 144 of those detections we provide firm associations of newly found AGNs based on statistical likelihood. More remarkably, we found a new population of  $\gamma$ -ray fields devoid of any compact radio source brighter than 2 mJy that lies outside the Galactic plane. We also provide a list of fields for which we found large-scale radio structures that are indicative of SNRs, H II regions, and radio-galaxy counterparts.

High-resolution radio follow-up observations are underway to cover all newly reported candidates for association, with which we expect to double the current number of new AGN associations.

We thank the anonymous referee for a thorough review that improved the quality of this publication. F.K.S., G.B.T., and L.P. acknowledge support by the NASA Fermi Guest Investigator program, grants NNX12A075G, NNX14AQ87G, and NNX15AU85G. The National Radio Astronomy Observatory is a facility of the National Science Foundation operated under cooperative agreement by Associated Universities, Inc. The Australia Telescope Compact Array & Long Baseline Array are part of the Australia Telescope National Facility, which is funded by the Commonwealth of Australia for operation as a National Facility managed by CSIRO. The authors also thank Jamie Stevens and Elaine Sadler for their support of the ATCA observations. F.K.S. dedicates this paper to his wife Mónica for her support and understanding leading to this publication.

This publication makes use of data products from the *Wide-field Infrared Survey Explorer*, which is a joint project of the University of California, Los Angeles, and the Jet Propulsion Laboratory/California Institute of Technology, and NEOWISE, which is a project of the Jet Propulsion Laboratory/California Institute of Technology. *WISE* and NEOWISE are funded by the National Aeronautics and Space Administration. This work made use of the Swinburne University of Technology software correlator, developed as part of the Australian Major National Research Facilities Programme and operated under licence. This research has made use of NASA's Astrophysics Data System and has made use of the NASA/IPAC Extragalactic Database (NED) which is operated by the Jet Propulsion Laboratory, California Institute of Technology, under contract with the National Aeronautics and Space Administration. This research has made use of data, software and/or web tools obtained from NASA's High Energy Astrophysics Science Archive Research Center (HEASARC), a service of Goddard Space Flight Center and the Smithsonian Astrophysical Observatory, of the SIMBAD database, operated at CDS, Strasbourg, France, and the TOPCAT software version

4.1<sup>15</sup> (Taylor 2005). The authors made use of the database CATS (Verkhodanov et al. 2007) of the Special Astrophysical Observatory.

*Facilities:* VLA, ATCA, VLBA, LBA, *Fermi*/LAT.

## References

- Abdo, A. A., Ajello, M., Allafort, A., et al. 2013, *ApJS*, **208**, 17
- Ajero, F., Ackermann, M., Ajello, M., et al. 2015, *ApJS*, **218**, 23
- Ackermann, M., Ajello, M., Allafort, A., et al. 2011, *ApJ*, **743**, 171
- Ackermann, M., Ajello, M., Allafort, A., et al. 2012, *ApJ*, **753**, 83
- An, T., Cui, Y.-Z., Gabányi, K. É., et al. 2016, *AN*, **337**, 65
- Bock, D. C.-J., Large, M. I., & Sadler, E. M. 1999, *AJ*, **117**, 1578
- Briggs, D. S. 1995, PhD thesis, The New Mexico Institute of Mining and Technology
- Gaia Collaboration, Brown, A. G. A., Vallenari, A., et al. 2016, *A&A*, **595**, 2
- Casandjian, J.-M., & Grenier, I. A. 2008, *A&A*, **489**, 849
- Clark, B. G. 1980, *A&A*, **89**, 377
- Clark, D. H., & Stephenson, F. R. 1977, *The historical supernovae* (New York: Pergamon Press)
- Condon, J. J., Cotton, W. D., Greisen, E. W., et al. 1998, *AJ*, **115**, 1693
- Frail, D. A., Mooley, K. P., Jagannathan, P., & Intema, H. T. 2016, *MNRAS*, **461**, 1062
- Gavriil, F. P., Kaspi, V. M., & Roberts, M. S. E. 2004, *AdSpR*, **33**, 592
- Greisen, E. W. 1990, in *Acquisition, Processing and Archiving of Astronomical Images*, ed. G. Longo & G. Sedmak (Napoli: Finito di stampare da Officine Grafiche Liguori), 125
- Hartman, R. C., Bertsch, D. L., Bloom, S. D., et al. 1999, *ApJS*, **123**, 79
- Intema, H. T., Jagannathan, P., Mooley, K. P., & Frail, D. A. 2017, *A&A*, **598**, 78
- Laffon, H., Smith, D. A., Guillemot, L. & for the Fermi-LAT Collaboration 2015, arXiv:1502.03251
- Mainzer, A., Bauer, J., Grav, T., et al. 2011, *ApJ*, **731**, 53
- Mauch, T., Murphy, T., Buttery, H. J., et al. 2003, *MNRAS*, **342**, 1117
- Murphy, T., Mauch, T., Green, A., et al. 2007, *MNRAS*, **382**, 382
- Perley, R. 2016, *Jansky Very Large Array Primary Beam Characteristics*, Tech. Rep. EVLA Memo #195, NRAO
- Petrov, L. 2013, *AJ*, **146**, 5
- Petrov, L. 2016, arXiv:1610.04951
- Petrov, L., & Kovalev, Y. Y. 2017, *MNRAS*, **467**, 71
- Petrov, L., Kovalev, Y. Y., Fomalont, E. B., & Gordon, D. 2008, *AJ*, **136**, 580
- Petrov, L., Mahony, E. K., Edwards, P. G., et al. 2013, *MNRAS*, **432**, 1294
- Petrov, L., Phillips, C., Bertarini, A., Murphy, T., & Sadler, E. M. 2011, *MNRAS*, **414**, 2528
- Readhead, A. C. S., Taylor, G. B., Pearson, T. J., & Wilkinson, P. N. 1996, *ApJ*, **460**, 634
- Schinzel, F. K., Petrov, L., Taylor, G. B., et al. 2015, *ApJS*, **217**, 4
- Taylor, M. B. 2005, in *ASP Conf. Ser. 347, Astronomical Data Analysis Software and Systems XIV*, ed. P. Shopbell, M. Britton, & R. Ebert (San Francisco, CA: ASP), 29
- Urquhart, J. S., Thompson, M. A., Moore, T. J. T., et al. 2013, *MNRAS*, **435**, 400
- Verkhodanov, O., Trushkin, S., Andernach, H., & Chernenkov, N. 2007, *HiA*, **14**, 636
- Wilkinson, P. N., Polatidis, A. G., Readhead, A. C. S., Xu, W., & Pearson, T. J. 1994, *ApJL*, **432**, L87
- Wright, E. L., Eisenhardt, P. R. M., Mainzer, A. K., et al. 2010, *AJ*, **140**, 1868

<sup>15</sup> <http://www.star.bris.ac.uk/~mbt/topcat/>